1-1-2005

Radiative decays of the Σ0(1385) and Λ+B95(1520) hyperons

S. Taylor

Angela Biselli
Fairfield University, abiselli@fairfield.edu

CLAS Collaboration

Published Citation

S. Taylor et al. [CLAS Collaboration], "Radiative decays of the Σ0(1385) and Λ+B95(1520) hyperons", Phys. Rev. C 71.5, 054609 (2005) [Erratum-ibid. C 72, 039902 (2005)] DOI: 10.1103/PhysRevC.71.054609

Radiative decays of the $\Sigma^0(1385)$ and $\Lambda(1520)$ hyperons

S. Taylor,[21] G. S. Mutchler,[32] G. Adams,[31] P. Ambrozewicz,[10] E. Anciant,[2] M. Anghinolfi,[16] B. Asavapibhop,[22] G. Asryan,[40] G. Audit,[2] H. Avakian,[35,15] H. Bagdasaryan,[27] J. P. Ball,[1] S. Barrow,[11] V. Batourine,[20] M. Battaglieri,[16] K. Beard,[19] M. Bektasoglu,[27] M. Bellis,[4] N. Benmouna,[13] B. L. Berman,[13] N. Bianchi,[15] A. S. Biselli,[4] S. Boiarinov,[35,18] B. E. Bonner,[32] S. Bouchigny,[17,35] R. Bradford,[4] D. Branford,[9] W. J. Briscoe,[13] W. K. Brooks,[35] S. Bültmann,[27] V. D. Burkert,[35] C. Butuceanu,[39] J. R. Calarco,[24] D. S. Carman,[26] B. Carnahan,[5] S. Chen,[11] P. L. Cole,[5,35] D. Cords,[35,*] P. Corvisiero,[16] D. Crabb,[38] H. Crannell,[5] J. P. Cummings,[31] E. De Sanctis,[15] R. DeVita,[16] P. V. Degtyarenko,[35] H. Denizli,[29] L. Dennis,[11] A. Deur,[35] K. V. Dharmawardane,[27] C. Djalali,[34] G. E. Dodge,[27] D. Doughty,[6,35] P. Dragovitsch,[11] M. Dugger,[1] S. Dytman,[29] O. P. Dzyubak,[34] H. Egiyan,[35] K. S. Egiyan,[40] L. Elouadrhiri,[35,6] A. Empl,[31] P. Eugenio,[11] R. Fatemi,[38] G. Feldman,[13] R. G. Fersch,[39] R. J. Feuerbach,[35] T. A. Forest,[27] H. Funsten,[39] M. Garçon,[2] G. Gavalian,[27] G. P. Gilfoyle,[33] K. L. Giovanetti,[19] E. Golovatch,[16,†] C. I. O. Gordon,[14] R. W. Gothe,[34] K. A. Griffioen,[39] M. Guidal,[17] M. Guillo,[34] N. Guler,[27] L. Guo,[35] V. Gyurjyan,[35] C. Hadjidakis,[17] R. S. Hakobyan,[5] J. Hardie,[6,35] D. Heddle,[6,35] F. W. Hersman,[24] K. Hicks,[26] I. Hleiqawi,[26] M. Holtrop,[24] J. Hu,[31] M. Huertas,[34] C. E. Hyde-Wright,[27] Y. Ilieva,[13] D. G. Ireland,[14] M. M. Ito,[35] D. Jenkins,[37] K. Joo,[7,38] H. G. Juengst,[13] J. D. Kellie,[14] M. Khandaker,[25] K. Y. Kim,[29] K. Kim,[20] W. Kim,[20] A. Klein,[27] F. J. Klein,[5] A. V. Klimenko,[27] M. Klusman,[31] M. Kossov,[18] V. Koubarovski,[31] L. H. Kramer,[10,35] S. E. Kuhn,[27] J. Kuhn,[4] J. Lachniet,[4] J. M. Laget,[2] J. Langheinrich,[34] D. Lawrence,[22] T. Lee,[24] Ji Li,[31] A. C. S. Lima,[13] K. Livingston,[14] K. Lukashin,[35,‡] J. J. Manak,[35] C. Marchand,[2] S. McAleer,[11] J. W. C McNabb,[28] B. A. Mecking,[35] J. J. Melone,[14] M. D. Mestayer,[35] C. A. Meyer,[4] K. Mikhailov,[18] M. Mirazita,[15] R. Miskimen,[22] V. Mokeev,[23] L. Morand,[2] S. A. Morrow,[2,17] V. Muccifora,[15] J. Mueller,[29] J. Napolitano,[31] R. Nasseripour,[10] S. Niccolai,[17,13] G. Niculescu,[19,26] I. Niculescu,[19,13] B. B. Niczyporuk,[35] R. A. Niyazov,[35,27] M. Nozar,[35] G. V. O'Rielly,[13] M. Osipenko,[16] A. I. Ostrovidov,[11] K. Park,[20] E. Pasyuk,[1] S. A. Philips,[13] N. Pivnyuk,[18] D. Pocanic,[38] O. Pogorelko,[18] E. Polli,[15] S. Pozdniakov,[18] B. M. Preedom,[34] J. W. Price,[3] Y. Prok,[38] D. Protopopescu,[14] L. M. Qin,[27] B. S. Raue,[10,35] G. Riccardi,[11] G. Ricco,[16] M. Ripani,[16] B. G. Ritchie,[1] F. Ronchetti,[15] G. Rosner,[14] P. Rossi,[15] D. Rowntree,[21] P. D. Rubin,[33] F. Sabatié,[2,27] C. Salgado,[25] J. P. Santoro,[37,35] V. Sapunenko,[35,16] R. A. Schumacher,[4] V. S. Serov,[18] A. Shafi,[13] Y. G. Sharabian,[35,40] J. Shaw,[22] S. Simionatto,[13] A. V. Skabelin,[21] E. S. Smith,[35] L. C. Smith,[38] D. I. Sober,[5] M. Spraker,[8] A. Stavinsky,[18] S. Stepanyan,[35] S. S. Stepanyan,[20] B. E. Stokes,[11] P. Stoler,[31] I. I. Strakovsky,[13] S. Strauch,[13] R. Suleiman,[21] M. Taiuti,[16] D. J. Tedeschi,[34] U. Thoma,[12,35] R. Thompson,[29] A. Tkabladze,[26] L. Todor,[33] C. Tur,[34] M. Ungaro,[7,31] M. F. Vineyard,[36,33] A. V. Vlassov,[18] K. Wang,[38] L. B. Weinstein,[27] H. Weller,[8] D. P. Weygand,[35] C. S. Whisnant,[34,§] M. Williams,[4] E. Wolin,[35] M. H. Wood,[34] A. Yegneswaran,[35] J. Yun,[27] and L. Zana[24]

(CLAS Collaboration)

[1]*Arizona State University, Tempe, Arizona 85287-1504, USA*

[2]*Commisariat à l'Energie Atomique-Saclay, Service de Physique Nucléaire, F-91191 Gif-sur-Yvette, Cedex, France*

[3]*University of California at Los Angeles, Los Angeles, California 90095-1547, USA*

[4]*Carnegie Mellon University, Pittsburgh, Pennsylvania 15213, USA*

[5]*Catholic University of America, Washington, DC 20064, USA*

[6]*Christopher Newport University, Newport News, Virginia 23606, USA*

[7]*University of Connecticut, Storrs, Connecticut 06269, USA*

[8]*Duke University, Durham, North Carolina 27708-0305, USA*

[9]*Edinburgh University, Edinburgh EH9 3JZ, United Kingdom*

[10]*Florida International University, Miami, Florida 33199, USA*

[11]*Florida State University, Tallahassee, Florida 32306, USA*

[12]*Physikalisches Institut der Universitaet Giessen, D-35392 Giessen, Germany*

[13]*The George Washington University, Washington, DC 20052, USA*

[14]*University of Glasgow, Glasgow G12 8QQ, United Kingdom*

[15]*Instituto Nazionali di fisica Nucleare, Laboratori Nazionali di Frascati, Frascati, Italy*

[16]*Instituto Nazionali di fisica Nucleare, Sezione di Genova, I-16146 Genova, Italy*

[17]*Institut de Physique Nucleaire ORSAY, Orsay, France*

[18]*Institute of Theoretical and Experimental Physics, Moscow, RU-117259, Russia*

[19]*James Madison University, Harrisonburg, Virginia 22807, USA*

[20]*Kyungpook National University, Daegu 702-701, South Korea*

[21]*Massachusetts Institute of Technology, Cambridge, Massachusetts 02139-4307, USA*

[22]*University of Massachusetts, Amherst, Massachusetts 01003, USA*

*Deceased.

†Current address: Moscow State University, General Nuclear Physics Institute, RU-119899 Moscow, Russia.

‡Current address: Catholic University of America, Washington, DC 20064.

§Current address: James Madison University, Harrisonburg, VA 22807.

[23]*Moscow State University, General Nuclear Physics Institute, RU-119899 Moscow, Russia*
[24]*University of New Hampshire, Durham, New Hampshire 03824-3568, USA*
[25]*Norfolk State University, Norfolk, Virginia 23504, USA*
[26]*Ohio University, Athens, Ohio 45701, USA*
[27]*Old Dominion University, Norfolk, Virginia 23529, USA*
[28]*Penn State University, University Park, Pennsylvania 16802, USA*
[29]*University of Pittsburgh, Pittsburgh, Pennsylvania 15260, USA*
[30]*Universita' di ROMA III, I-00146 Roma, Italy*
[31]*Rensselaer Polytechnic Institute, Troy, New York 12180-3590, USA*
[32]*Rice University, Houston, Texas 77005-1892, USA*
[33]*University of Richmond, Richmond, Virginia 23173, USA*
[34]*University of South Carolina, Columbia, South Carolina 29208, USA*
[35]*Thomas Jefferson National Accelerator Facility, Newport News, Virginia 23606, USA*
[36]*Union College, Schenectady, New York 12308, USA*
[37]*Virginia Polytechnic Institute and State University, Blacksburg, Virginia 24061-0435, USA*
[38]*University of Virginia, Charlottesville, Virginia 22901, USA*
[39]*College of William and Mary, Williamsburg, Virginia 23187-8795, USA*
[40]*Yerevan Physics Institute, 375036 Yerevan, Armenia*
(Received 16 July 2004; revised manuscript received 18 January 2005; published 31 May 2005)

The electromagnetic decays of the $\Sigma^0(1385)$ and $\Lambda(1520)$ hyperons were studied in photon-induced reactions $\gamma p \to K^+\Lambda(1116)\gamma$ in the Large Acceptance Spectrometer detector at the Thomas Jefferson National Accelerator Facility. We report the first observation of the radiative decay of the $\Sigma^0(1385)$ and a measurement of the $\Lambda(1520)$ radiative decay width. For the $\Sigma^0(1385) \to \Lambda(1116)\gamma$ transition, we measured a partial width of $479 \pm 120(\text{stat})^{+81}_{-100}(\text{sys})$ keV, larger than all of the existing model predictions. For the $\Lambda(1520) \to \Lambda(1116)\gamma$ transition, we obtained a partial width of $167 \pm 43(\text{stat})^{+26}_{-12}(\text{sys})$ keV.

DOI: 10.1103/PhysRevC.71.054609 PACS number(s): 14.20.Jn, 13.30.Ce, 13.40.Hq

I. INTRODUCTION

The low-lying neutral excited-state hyperons $\Sigma^0(1385)$, $\Lambda(1405)$, and $\Lambda(1520)$ were discovered in the 1960s, but their quark wave functions are still not well understood, and experimental studies of their properties have been scarce since the early 1980s. The electromagnetic decays of baryons produced in photon reactions provide an especially clean method of probing their wave functions. Baryons with a strange quark have an additional degree of freedom that aids in the study of multiplet mixing and non-3-quark admixtures. Recently there has been a renewal of interest in this field, e.g., electroproduction of the $\Lambda(1520)$ [1]. This paper reports the results of a non-model-dependent measurement of the radiative decay of $\Sigma^0(1385)$ and $\Lambda(1520)$.

The nonrelativistic quark model (NRQM) of Isgur and Karl [2] has been remarkably successful in predicting the masses and widths of N^* and Δ^* states, but less successful in the strange sector. Several competing models for hyperon wave functions have been proposed. Measuring the transitions $Y \to \Lambda(1116)\gamma$ and $Y \to \Sigma(1193)\gamma$ provides a means of differentiating between these models. Calculations have been done in the framework of NRQM [3,4], a relativized constituent quark model (RCQM) [5], a chiral constituent quark model (χCQM) that includes electromagnetic exchange currents between the quarks [6], the MIT bag model [3], the chiral bag model [7], the bound-state soliton model [8], a three-flavor generalization of the Skyrme model that uses the collective approach instead of the bound-state approach [9,10], an algebraic model of hadron structure [11], heavy baryon chiral perturbation theory (HBχPT) [12], and the $1/N_c$ expansion of QCD [13]. The radiative widths, in keV, are tabulated in Table I. The $\Delta \to p\gamma$ width is included for comparison.

The photon decay spectrum of the low-lying excited-state hyperons is shown in Fig. 1. The widths given in Table I can be qualitatively estimated because of SU(3) symmetry. The $\Lambda(1116)$ and the $\Sigma^0(1193)$ are in the $S = 1/2^+$ SU(3) octet and the $\Sigma^0(1385)$ is in the $S = 3/2^+$ SU(3) decuplet. The $\Lambda(1116)$ has the two light quarks in the s orbital in a spin $S = 0$, isospin $T = 0$ configuration. The $\Sigma^0(1193)$ and the $\Sigma^0(1385)$ have the light quarks in a spin $S = 1, T = 1$ configuration. All three hyperons have the strange quark in the s orbital. Decuplet to octet radiative decays are dominated by an M1 transition with a spin flip of one quark. The SU(3) model prediction of the ratio $\Sigma^* \to \Sigma\gamma$ to the $\Sigma^* \to \Lambda\gamma$ is $\sim\frac{1}{6}$ times kinematic factors. This, plus the fact that most of the constituent quark model calculations [3–6,14] listed in Table I used the impulse approximation, leads to a very narrow range of predictions, (265–273 keV) for the $\Sigma^* \to \Lambda\gamma$ reaction and (17.4–23 keV) for the $\Sigma^* \to \Sigma\gamma$ reaction. The $\Lambda(1405)$ and $\Lambda(1520)$ have light quarks in the s orbital with $S = 0, T = 0$ and the strange quark in a $p\frac{1}{2}$ and $p\frac{3}{2}$ orbital, respectively. The radiative decays $\Lambda(1520) \to \Sigma^*, \Sigma$ and $\Lambda(1405) \to \Sigma^*, \Sigma$ require that the strange quark make a transition from a p orbital to an s orbital with a simultaneous spin flip of one of the light quarks. These transitions are thus forbidden by the one-body nature of the electromagnetic operator. They can proceed only by means of configuration mixing introduced by, e.g., the QCD

TABLE I. Theoretical predictions and experimental values for the radiative widths (in keV) for the transitions $Y \to \Lambda(1116)\gamma$ and $Y \to \Sigma(1193)\gamma$. Some models have multiple predictions that depend on different assumptions. For comparison the predictions and experimental value are quoted for the $\Delta(1232) \to p\gamma$ transition.

Model	$\Delta(1232)$	$\Sigma^0(1385)$		$\Lambda(1405)$		$\Lambda(1520)$	
	$p\gamma$	$\Lambda(1116)\gamma$	$\Sigma^0(1193)\gamma$	$\Lambda(1116)\gamma$	$\Sigma^0(1193)\gamma$	$\Lambda(1116)\gamma$	$\Sigma^0(1193)\gamma$
NRQM [3,4]	360 [14]	273	22	200	72	156	55
RCQM [5]		267	23	118	46	215	293
χCQM [6]	350	265	17.4				
MIT bag [3]		152	15	60, 17	18, 2.7	46	17
Chiral bag [7]				75	1.9	32	51
Soliton [8]		243, 170	19, 11	44, 40	13, 17		
Skyrme [9,10]	309–348	157–209	7.7–16				
Algebraic model [11]	343.7	221.3	33.9	116.9	155.7	85.1	180.4
HBχPT [12][a]	(670–790)	290–470	1.4–36				
$1/N_c$ expansion [13]		298 ± 25	24.9 ± 4.1				
Previous experiments	640–720 [30]	<2000 [22]	<1750 [22]	27 ± 8 [19]	10 ± 4 [19]	33 ± 11 [17]	47 ± 17 [17]
					23 ± 7 [19]	134 ± 23 [16]	
						$159 \pm 33 \pm 26$ [18]	
This experiment		$479 \pm 120^{+81}_{-100}$				$167 \pm 43^{+26}_{-12}$	

[a]The results for HBχPT [12] are normalized to the quoted empirical range (in parentheses) for the $\Delta \to p\gamma$ transition.

hyperfine interaction, which leads to a wider range of model predictions. This is explained in more detail in an excellent review of the experimental and theoretical situation in [15].

Experimental measurements have been sparse. The results are tabulated in Table I. The $\Lambda(1520) \to \Lambda\gamma$ transition has been measured by Mast *et al*. [16], who used a K^- beam with a liquid-hydrogen bubble chamber; by Bertini *et al*. [17] with a liquid-hydrogen target viewed by a NaI detector; and by Antipov *et al*. [18], who used a high-energy proton beam on carbon and copper targets. Antipov *et al*. measured the K^+, p and π^- in a magnetic spectrometer and detected the decay photons by using an electromagnetic calorimeter. These are the only direct measurements in the literature. Burkhardt and Lowe [19] extracted model-dependent branching ratios for $\Lambda(1405)$ radiative decay from the kaon-proton capture data of Whitehouse *et al*. [20]. The radiative decay of the $\Sigma^0(1385)$ has never been observed (Meisner [21] reports one event); only upper limits for the branching ratios have been established [22].

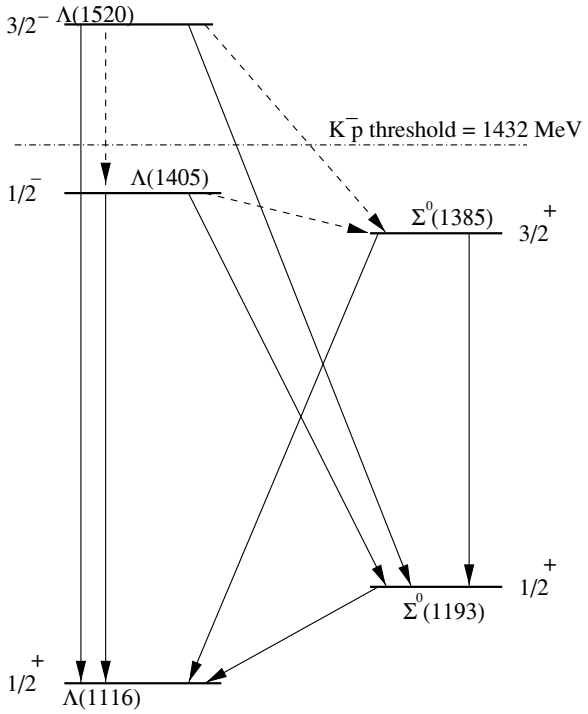

FIG. 1. Photon decay spectrum of low-lying excited-state hyperons. The transitions shown as dashed lines are suppressed.

II. EXPERIMENT

In the current experiment, the low-lying excited-state hyperons were studied in the reaction $\gamma p \to K^+ p \pi^- X$ with the Large Acceptance Spectrometer (CLAS) in Hall B at the Thomas Jefferson National Accelerator Facility. The data were from the G1C running period, September to October 1999. The primary electron beam was converted to a photon beam with a thin radiator of 10^{-4} radiation lengths. The scattered electron was momentum-analyzed by a photon tagging spectrometer [23] with a resolution of $\Delta E/E = 10^{-3}$. Photons were tagged over a range of 20%–95% of the incident electron-beam energy. The electron-beam energies were 2.445, 2.897, and 3.115 GeV, and the currents were typically 6 nA. The target was liquid hydrogen in a cylindrical cell of 17.9-cm length and 2-cm radius. The CLAS detector [24] consisted of six individually instrumented segments, each consisting of three layers of drift chambers and a shell of 48 time-of-flight scintillators. Six superconducting magnets provided a toroidal magnetic field, with negative particles bent toward the beam direction. The trigger consisted of a triple coincidence among the photon tagger, the time-of-flight system, and a small scintillation detector (the "Start Counter" [25]) surrounding

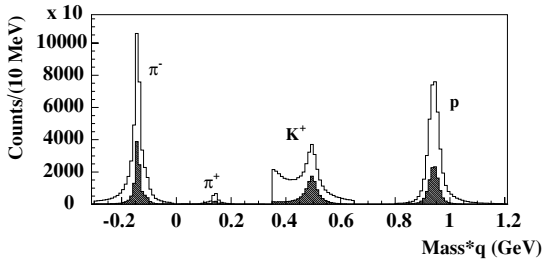

FIG. 2. Particle identification: Hadron mass from TOF and momentum information multiplied by the sign of the charge of the particle. The shaded curve is the mass spectrum after the particle identification cuts.

the target scattering chamber. Only one charged particle in the CLAS was required in the trigger for accommodating the six experiments that were running simultaneously. A total of 1420M triggers were collected at 2.445 GeV, 845M at 2.897 GeV, and 2280M at 3.115 GeV.

A. Particle identification

Charged hadrons were identified by use of momentum and time-of-flight information. The processed data files were filtered for events containing one K^+, one π^-, and one proton track in coincidence with the incident tagged photon. Kaon candidates were chosen with a broad range in mass (0.35–0.65 GeV). The π^- candidates were selected with a mass range of <0.3 GeV and proton candidates with a range of 0.8–1.2 GeV. A minimum momentum cut of 0.3 GeV/c was applied for the kaons and protons and 0.1 GeV/c for the pions. The hadron mass spectrum for events that survive the filter is shown in Fig. 2. The kaon peak sits on top of a large background because of high momentum pions with poorly determined mass.

To further refine the kaon identification, the difference Δt between the time at the target for the kaon candidate and what it would be for a true kaon was computed:

$$\Delta t = (t_{\mathrm{TOF}} - t_{\mathrm{vert}}) \left(1 - \sqrt{\frac{p^2 + M_{K^+}^2}{p^2 + M_{\mathrm{calc}}^2}} \right), \tag{1}$$

$$M_{\mathrm{calc}}^2 = \frac{p^2}{\gamma^2 \beta^2}, \tag{2}$$

where $t_{\mathrm{TOF}} - t_{\mathrm{vert}}$ is the flight time between the interaction vertex and the time-of-flight array. We require $|\Delta t| < 0.67$ ns. Because the experiment consists of two physically separate systems, the tagger and the CLAS detector, we require that the time at the interaction vertex measured by the two systems agree to within 5% of the flight time between the start counter and the TOF paddles.

The CLAS detector does not cover the full angular range in θ or ϕ. Some angular regions are shadowed by the toroidal coils. The shadow region broadens in ϕ as a function of decreasing θ as seen from the center of the target. All tracks were required to be in the region of well-understood acceptance by application of a fiducial cut of the form

$$\theta > 4.0 + \frac{510.58}{(30 - \phi)^{1.5518}}, \tag{3}$$

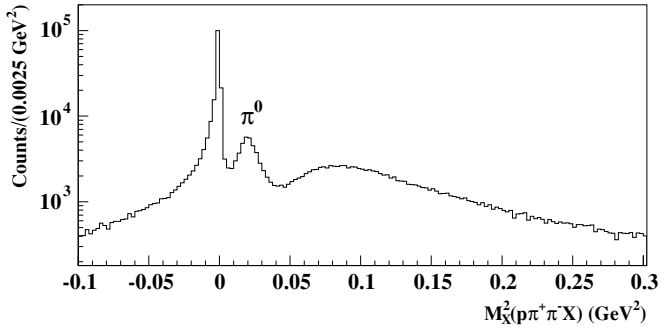

FIG. 3. Pion contamination: Mass squared (M_X^2) for the $\gamma p \to p\pi^+\pi^-(X)$ reaction, where the π^+ was a potentially misidentified kaon.

where ϕ is the azimuthal angle folded onto the range 0–30°. We also require $\phi < 26°$.

Some of the kaon events are really misidentified π^+. This can be seen in Fig. 3, where all events are plotted assuming that all kaon candidates are really misidentified π^+ and compute the missing mass squared for the reaction $\gamma p \to p\pi^+\pi^-(X)$. The prominent spike at zero mass squared indicates $\gamma p \to p\pi^+\pi^-$ contamination and a π^0 peak is clearly evident but at a much reduced level. The expected distribution for good K^+ events goes to zero for zero $p\pi^+\pi^-$ missing mass squared. We require the missing mass squared from this calculation to be greater than 0.01 GeV^2 to eliminate, for example, $\rho \to \pi^+\pi^-$ contamination. We did not cut above the π^0 peak in Fig. 3 because that would have cut into the good K^+ events. The hadron mass spectrum after all of the above cuts have been applied are shown as the shadowed histogram in Fig. 2.

The kaon momentum is corrected for average dE/dx losses in the target material, target wall, carbon epoxy pipe, and the start counter, depending on the position of the primary vertex, which is approximated by the intersection of the proton and kaon tracks. The ground state Λ is sufficiently long lived that it decays a measurable distance from the primary vertex. The secondary vertex is determined by the intersection of the proton and π^- tracks. The proton and π^- tracks are corrected for average dE/dx losses according to the position of the secondary vertex.

The four-momentum of the $\Lambda(1116)$ was reconstructed from the proton and π^- four-momenta (Fig. 4). The Gaussian resolution of the Λ peak is about $\sigma = 1.3$ MeV, consistent with

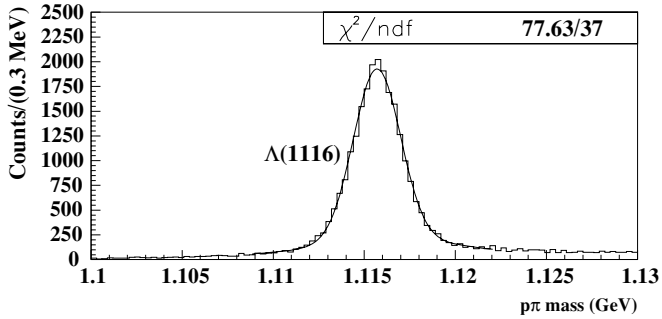

FIG. 4. Λ identification: proton-π^- invariant mass. The number of degrees of freedom (ndf) were 37.

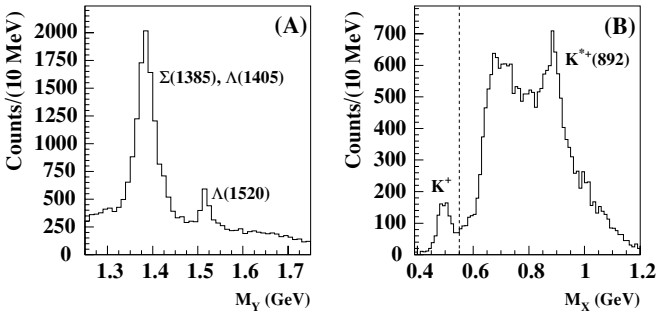

FIG. 5. (A) Missing mass for the reaction $\gamma p \to K^+(X)$. (B) Missing mass for the reaction $\gamma p \to \Lambda(X)$.

the instrumental resolution. The excited-state hyperon mass spectrum for the region between 1.25 and 1.75 GeV, requiring the $p\pi^-$ invariant mass to be in the range 1.112–1.119 GeV, is shown in Fig. 5(A). Figure 5(B) shows the mass M_X from the reaction $\gamma p \to \Lambda(X)$. A clear peak at the mass of the $K^*(892)$ is seen. The peak at the K^+ mass is due to accidentals under the TOF peak. This background is eliminated by the requirement that $M_X > 0.55$ GeV. Figure 6 shows the missing mass squared for the reaction $\gamma p \to K^+\Lambda(X)$ after the foregoing cuts have been applied. A prominent peak shows up at $M^2_{\pi^0}$ and a smaller peak at zero missing mass squared. The counts above the π^0 peak are typically due to $\gamma p \to K^+\Sigma^0(X)$.

B. Kinematic fitting

A better approximation to the primary and secondary vertices can be found by use of kinematic fitting. We used the Lagrange multiplier method [26]. The unknowns are divided into a set of measured variables ($\vec{\eta}$) and a set of unmeasured variables ($\vec{\xi}$) such as the missing momentum or the four-vector for a decay particle. For each constraint equation a Lagrange multiplier λ_i is introduced. We minimize

$$\chi^2(\vec{\eta}, \vec{\xi}, \vec{\lambda}) = (\vec{\eta}_0 - \vec{\eta})^T V^{-1}(\vec{\eta}_0 - \vec{\eta}) + 2\vec{\lambda}^T \vec{f} \qquad (4)$$

by differentiating χ^2 with respect to all the variables, linearizing the constraint equations and iterating. Here $\vec{\eta}_0$ is a vector containing the initial guesses for the measured quantities and V is the covariance matrix comprising the estimated errors on the measured quantities. We iterate until the difference in magnitude between the current χ^2 and the previous value is

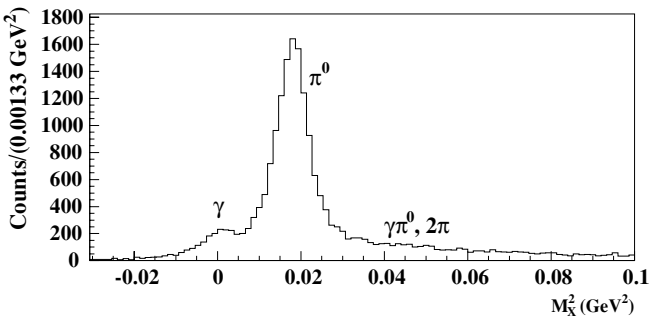

FIG. 6. Missing mass squared for the reactions $\gamma p \to K^+\Lambda(X)$.

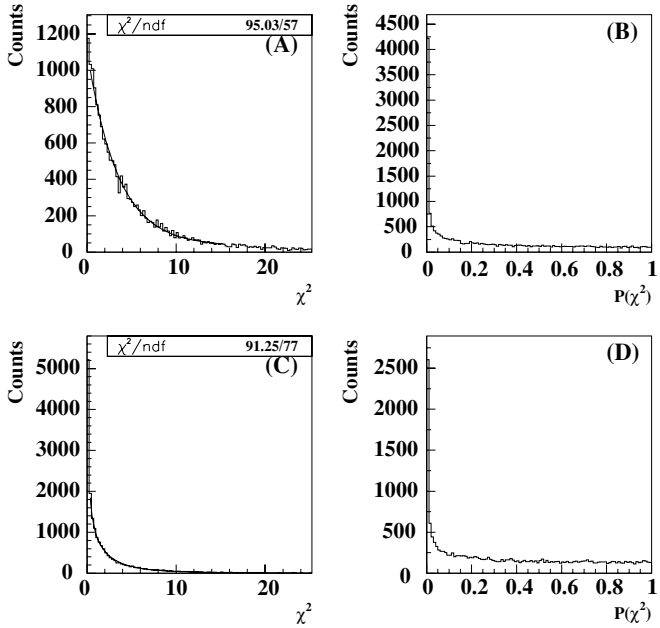

FIG. 7. χ^2 and confidence level distributions for (A), (B) the $\Lambda \to p\pi^-$ fit and (C), (D) the $K^+\Lambda$ vertex fit.

$\leqslant 0.001$. The covariance matrix V for each track returned by the tracking code does not contain the effects of multiple scattering and energy loss in the target cell, the carbon epoxy pipe, or the start counter. To correct for this we apply multiple scattering and energy loss corrections to the diagonal matrix elements.

The first step in the fitting procedure is to fit the proton and π^- tracks with the Λ hypothesis. This is a 2C fit. There are six unknowns ($\vec{p}_\Lambda, \vec{r}_{V2}$) and eight constraint equations;

$$\vec{f} = \begin{bmatrix} E_p + E_\pi - E_\Lambda \\ \vec{p}_p + \vec{p}_\pi - \vec{p}_\Lambda \\ (y - y_\pi)p^z_\pi - (z - z_\pi)p^y_\pi \\ (x - x_\pi)p^z_\pi - (z - z_\pi)p^x_\pi \\ (y - y_p)p^z_p - (z - z_p)p^y_p \\ (x - x_p)p^z_p - (z - z_p)p^x_p \end{bmatrix} = \vec{0}. \qquad (5)$$

The χ^2 distribution for this fit is shown in Fig. 7(A) and the confidence level plot is shown in Fig. 7(B). The curve is the result of a fit to the histogram by use of the function form of a χ^2 distribution with 2 degrees of freedom plus a flat background term. Explicitly,

$$f(\chi^2) = \frac{P_1}{2} e^{-P_2\chi^2/2} + P_3. \qquad (6)$$

The fit result ($P_2 = 0.558$) suggests that we are underestimating the errors in the proton and π^- tracks, but the shape is close to the expected shape. The confidence level is given by

$$CL = \int_{\chi^2}^{\infty} f(z; n)dz, \qquad (7)$$

where $f(z; n)$ is the χ^2 probability density function with n degrees of freedom.

The second step is to use these kaon and lambda tracks to obtain a better primary vertex. This is a 1C fit. There are three unknowns ($\vec{r}_{V1}$) and four constraint equations. The χ^2

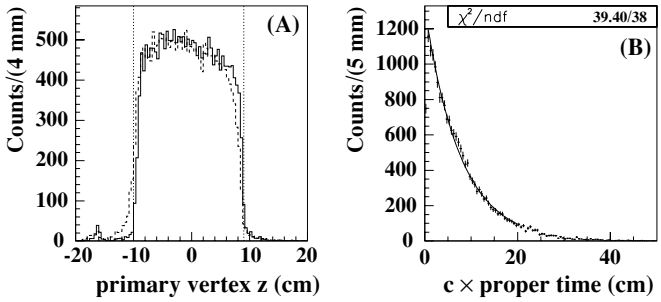

FIG. 8. (A) The z position of primary vertex. Solid histogram: $K\Lambda$ fit; dashed histogram: Kp fit. (B) Lambda decay proper time in units of centimeters. The excited-state hyperon mass was greater than 1.25 GeV for both plots.

distribution for this fit is shown in Fig. 7(C), and the confidence level plot is shown in Fig. 7(D). The curve in Fig. 7(C) is the result of a fit to the histogram by use of the functional form of a χ^2 distribution with 1 degree of freedom plus a flat background term. Explicitly,

$$f(\chi^2) = \frac{P_1}{\sqrt{2}\Gamma(1/2)} \frac{e^{-P_2\chi^2/2}}{\sqrt{\chi^2}} + P_3, \tag{8}$$

with a fit result of $P_2 = 0.507$. We require that the probability of the $\Lambda \to p\pi^-$ fit and the primary vertex fit be $\leqslant 0.5\%$ of exceeding χ^2 for an ideal χ^2 distribution. The improved kaon and lambda 4-vectors are used to compute the excited-state hyperon mass spectrum and the missing mass squared.

Figure 8(A) compares the z position of the primary vertex from the improved fitting procedure to the naive kaon-proton result. We apply a target z-position cut for the primary vertex between -10.0 and $+9.0$ cm and a radial cut of 2 cm. These cuts were chosen to ensure that the primary event came from the target region. The proper time of the Λ decay is plotted in Fig. 8(B). An exponential fit to the data gives a decay constant of 7.62 ± 0.09 cm, which is comparable to the Particle Data Group value of 7.89 ± 0.06 cm. To verify that the target walls do not make a significant contribution to our yields, we applied the analysis procedure described above to the empty-target data. For the empty target runs the beam current ranged between 10 and 24 nA and averaged about 15 nA. The results from analyzing about 33 million empty-target events (corresponding to approximately $\frac{1}{3}$ of the target full integrated photon flux) are shown in Fig. 9. We obtained 25 $\Lambda(1116)$ candidates within the proton-π^- invariant mass range of 1.112–1.119 GeV [Fig. 9(A)]. The z distribution is shown in Fig. 9(B). The hyperon mass distribution for those events satisfying the vertex cut is shown in Fig. 9(C). Figure 9(D) shows the missing mass squared distribution for hyperon masses in the 1.34–1.43-GeV range. There are no counts near zero missing mass squared and only two near $m^2_{\pi^0}$. Both of these counts have z and r positions within the target volume. They correspond to interactions with the residual (cold) hydrogen gas in the target. From this we conclude that the background, because of interactions with the walls of the target cell, is negligible.

To achieve γ/π^0 separation, the events were sorted according to topology by use of kinematic fits with two

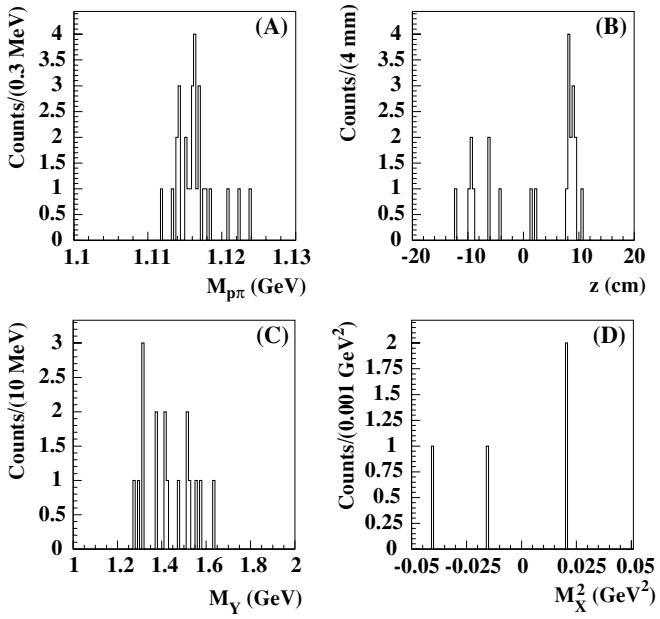

FIG. 9. Empty target results. (A) Proton π invariant mass, (B) vertex z position, (C) hyperon mass, (D) missing mass squared for $M_Y = 1.34$–1.43 GeV.

hypotheses:

$$R1\colon\ \gamma p \to K^+\Lambda\pi^0\ 1\text{C},$$
$$R2\colon\ \gamma p \to K^+\Lambda\gamma\ 1\text{C}.$$

The corresponding constraint equations are

$$\vec{f} = \begin{bmatrix} E_{\text{beam}} + M_p - E_K - E_\Lambda - E_X \\ \vec{p}_{\text{beam}} - \vec{p}_K - \vec{p}_\Lambda - \vec{p}_X \end{bmatrix} = \vec{0}. \tag{9}$$

Here X is a missing π^0 or a missing γ.

The χ^2 distributions for reactions $R1$ and $R2$ are shown in Figs. 10(A) and 10(C), respectively. The hyperon mass range was 1.25–1.75 GeV. The corresponding confidence levels plots are shown in Figs. 10(B) and 10(D). For $R1$ we obtain the expected shape for a χ^2 distribution with 1 degree of freedom. For $R2$ the χ^2 values indicates that the radiative decay hypothesis is inconsistent with most of the events. The dashed curve in Fig. 10(D) is the confidence level for hypothesis $R2$ for those events that do not satisfy hypothesis $R1$ at the 5% level. We now see a shape consistent with a χ^2 distribution with 1 degree of freedom.

Figure 11 shows the missing mass squared distributions for a representative set of χ^2 cuts. For the purpose of the plot, we require $\chi^2_{R1} \geqslant 3.841$ and $\chi^2_{R2} < 3.841$ to isolate the radiative channel [case 11(B)]. To isolate the pion channel [case 11(A)], we require $\chi^2_{R1} < 3.841$ and $\chi^2_{R2} \geqslant 3.841$. Case 11(C) is the "ambiguous" case in which both $\chi^2_{R1} < 3.841$ and $\chi^2_{R2} < 3.841$. Case 11(D) consists of those events that do not agree with either the radiative channel or the pion channel, for which $\chi^2_{R1} \geqslant 3.841$ and $\chi^2_{R2} \geqslant 3.841$. For a 1C fit $\chi^2 = 3.841$ corresponds to a 5% probability of exceeding χ^2 for an ideal χ^2 distribution. The ambiguous events are most likely to be $\gamma p \to K^+\Lambda\pi^0$ events. Case 11(D) events are most likely be $\gamma p \to K^+\Sigma^0\pi^0$ events. Figure 12 shows the corresponding

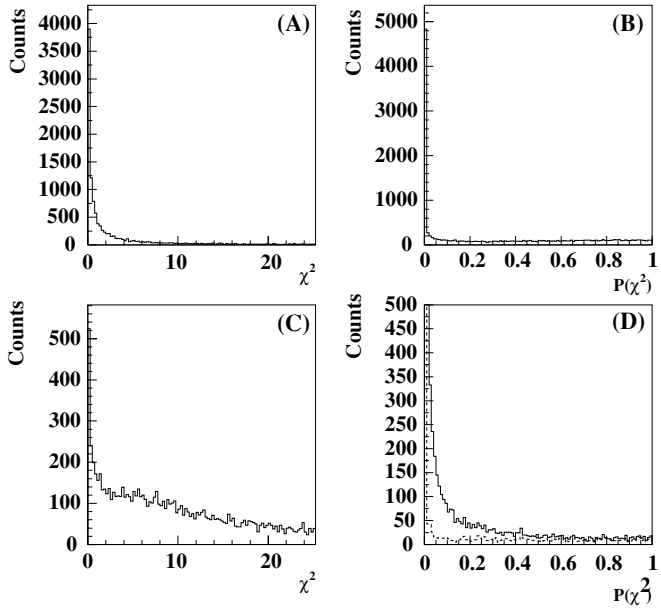

FIG. 10. χ^2 and confidence level distributions for the two reactions (A), (B) $R1$ and (C), (D) $R2$. The dashed curve in (D) is the $R2$ confidence level with the $R1$ reaction vetoed with $\chi^2 = 3.841$.

hyperon mass spectra. Figure 12(A) is dominated by the $\Sigma^0(1385) \to \Lambda\pi^0$ channel, for which the branching ratio is ~88% [30]. We calculated the $\Sigma(1385)$ radiative transition relative to this channel. The $\Lambda(1520)$ peak shows up in Fig. 12(D) because of the decay channels $\Lambda(1520) \to \Sigma^0\pi^0$ (BR = 14%) and $\Lambda(1520) \to \Lambda\pi\pi$ (BR = 10%).

C. Double bremsstrahlung

The γ channel does not show the structure expected from hyperon photon decays. The structure was found to be

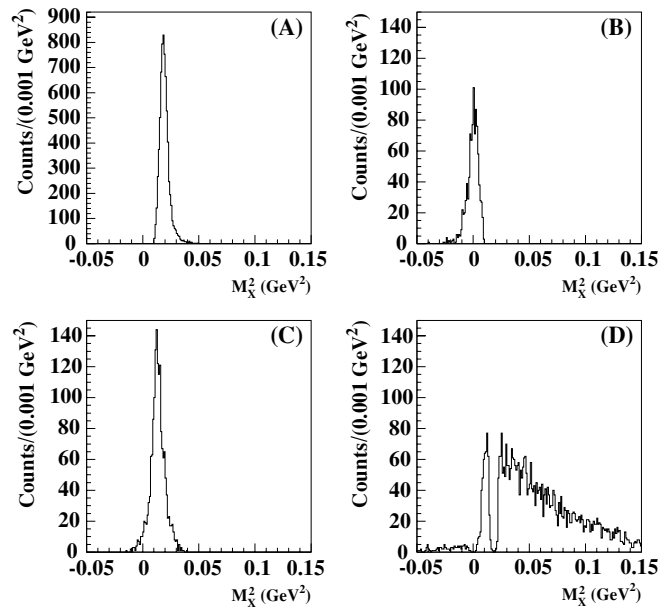

FIG. 11. Missing mass squared distributions for $\chi^2_{\rm HIGH} = \chi^2_{\rm LOW} = 3.841$. Cases (A)–(D) are explained in the text.

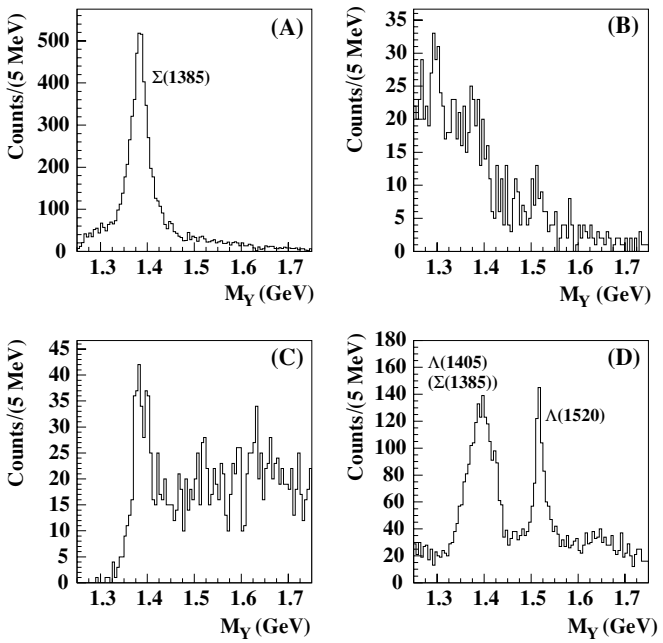

FIG. 12. Hyperon mass distributions for $\chi^2_{\rm HIGH} = \chi^2_{\rm LOW} = 3.841$. Cases (A)–(D) are explained in the text.

masked by a background resulting from double bremsstahlung in the radiator. The reaction $\gamma_1 + \gamma_2 p \to K^+\Lambda + \gamma_1$ can mimic the reaction $\gamma p \to K^+\Lambda\gamma$. However, in this case the missing momentum from the reaction $\gamma p \to K^+\Lambda(X)$ points along the $+z$ direction (along the beam). This can also happen if the event is accidental or inefficiencies in the tagger plane allow the wrong electron to be selected. This problem is illustrated in Fig. 13. Figure 13(A) shows the off-z-axis momentum $p_\perp^2 = p_x^2 + p_y^2$ for the candidate missing particle.

This misidentification should happen for ground-state $\Sigma^0(1193)$ production as well. A subset of the data filtered on the hyperon mass region between 1.0 and 1.25 GeV was used to isolate $\Sigma^0(1193)$ events. The σ from a Gaussian fit to the Σ^0 peak is about 6.6 MeV, corresponding to a full width at half maximum of $\Gamma = 2.354\sigma = 15.6$ MeV. This is a measure of the hyperon mass resolution. Apart from the hyperon mass range, the same set of cuts was used to analyze these data as for the excited-state sample. Figure 13(C) shows the distribution in $p_\perp^2$ for this data set. Figures 13(B) and 13(D) compare the effect of two choices for the $p_\perp^2$ cut on the hyperon mass distribution for the case in which the γ channel is favored. The histograms show the distributions in hyperon mass for those events that were cut out. Histograms 13(B) and 13(D) both look like exponentially falling distributions. Figure 14 shows the corresponding hyperon mass spectra after the $p_\perp^2 = 0.015$ GeV^2 cut is applied. The histogram now shows the expected structure for the $\Sigma(1385) \to \Lambda\gamma$ and $\Lambda(1520) \to \Lambda\gamma$ reactions. Comparison with Fig. 12(A) shows that this cut also reduces the number of $\Lambda\pi^0$ events seen. The Monte Carlo (MC) simulation III is used to correct for this reduction. The $p_\perp^2 = 0.015$ GeV^2 cut is used for the rest of the analysis.

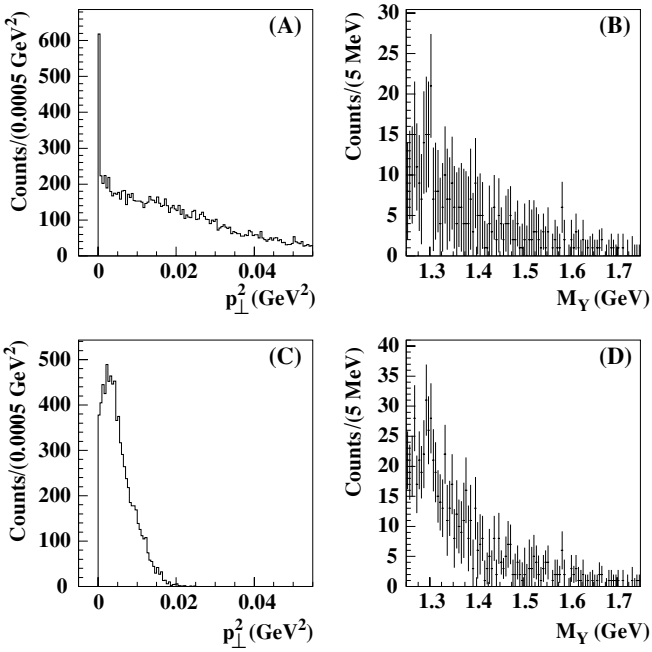

FIG. 13. Effect of $p_\perp^2$ cut on γ channel. (A) The $p_\perp^2$ momentum spectrum for $K^+\Lambda(X)$ events, (B) the γ-channel cut distibution for a 0.0004-GeV^2 cut, (C) the $p_\perp^2$ momemtum spectrum for $K^+\Sigma^0(X)$ events, (D) the γ-channel cut distibution for a 0.015-GeV^2 cut.

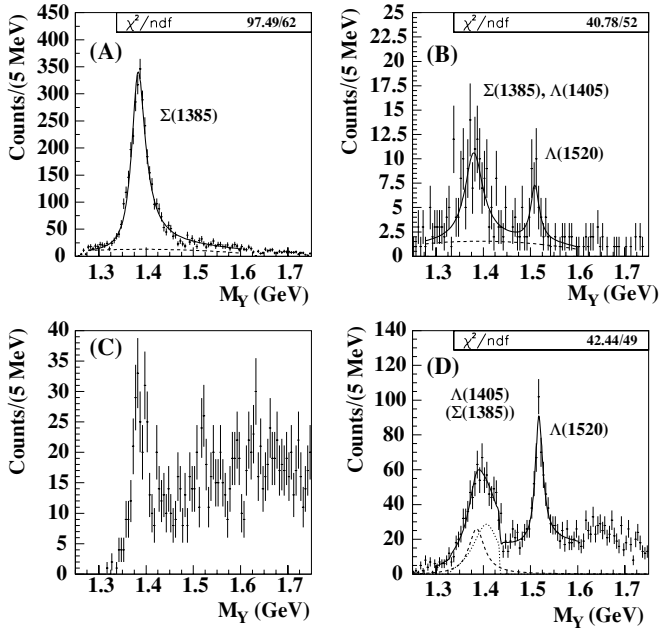

FIG. 14. Hyperon mass distributions for $\chi^2_{\rm LOW} = \chi^2_{\rm HIGH} = 3.841$ with $p_\perp^2 = 0.015$-GeV^2 cut. The labels are explained in the text. The yield of $\Lambda\pi^0$ and $\Lambda\gamma$ events in (A) and (B) were extracted by fitting the data with a relativistic Breit-Wigner (solid curve) and a polynomial background (dashed curve). In (D) the dashed histogram shows the contribution that is due to the $\Sigma(1385)$ alone. The dotted histogram is the $\Lambda(1405)$ contribution alone, with the M-matrix parametrization used for the shape.

III. ACCEPTANCE

A detailed MC simulation of the CLAS detector was performed with GEANT 3.21 for each of the three electron-beam energies. Table II lists the set of reactions for which we generated events. The experimental photon energy distribution was used to determine the energies of the incident photons in the simulation. Relativistic Breit-Wigner shapes were used for the $\Sigma(1385)$, $\Lambda(1520)$, and K^* mass distributions. For the $\Lambda(1520)$ the exponential slope for the t dependence was 2.0 GeV^{-2}. The angular distribution for the radiative decay of the $\Lambda(1520)$ in its rest frame was taken to be proportional to $5–3\cos^2\theta$ according to the result obtained by Mast *et al.* [16]. The same distribution was used for the $\Sigma\pi$ channels and for the $\Sigma(1385)$ decays. The model of Nacher *et al.* [27] with a flat angular distribution was used for the $\Lambda(1405)$ decay channels.

The incident photon energy dependence and t dependence were adjusted to fit the data for the $\Sigma(1385)$ reactions independently for each of the electron-beam energies. The data and MC were cut on the Y^* mass range of 1.34–1.43 GeV and

TABLE II. Acceptances (in units of 10^{-3}) for the channels used in the calculation of the branching ratios. Here $\chi^2_{\rm HIGH} = \chi^2_{\rm LOW} = 3.841$. The uncertainties are statistical only.

Reaction	A_π	A_γ	$A_{\gamma\pi}$
$\Lambda(1405) \to \Sigma^0\pi^0$	0.083 ± 0.004	0.0007 ± 0.0004	0.658 ± 0.012
$\Lambda(1405) \to \Sigma^+\pi^-$	0.088 ± 0.005	0.0038 ± 0.0009	0.013 ± 0.002
$\Lambda(1405) \to \Lambda\gamma$	0.008 ± 0.003	0.946 ± 0.028	0.098 ± 0.009
$\Lambda(1405) \to \Sigma^0\gamma$	0.585 ± 0.019	0.380 ± 0.015	0.837 ± 0.023
$\Sigma(1385) \to \Lambda\pi$	0.905 ± 0.010	0.011 ± 0.001	0.086 ± 0.003
$\Sigma(1385) \to \Sigma^+\pi^-$	0.050 ± 0.002	0.0018 ± 0.0005	0.00564 ± 0.0008
$\Sigma(1385) \to \Lambda\gamma$	0.012 ± 0.002	1.309 ± 0.022	0.105 ± 0.006
$\Sigma(1385) \to \Sigma^0\gamma$	0.548 ± 0.016	0.24 ± 0.01	0.99 ± 0.02
$\Lambda(1520) \to \Lambda\gamma$		1.388 ± 0.027	0.0010 ± 0.0007
$\Lambda(1520) \to \Sigma^0\gamma$		0.087 ± 0.006	0.586 ± 0.016
$\Lambda(1520) \to \Lambda\pi^0\pi^0$		0	0.0099 ± 0.0016
$\Lambda(1520) \to \Sigma^0\pi^0$		0.0006 ± 0.0004	0.681 ± 0.014

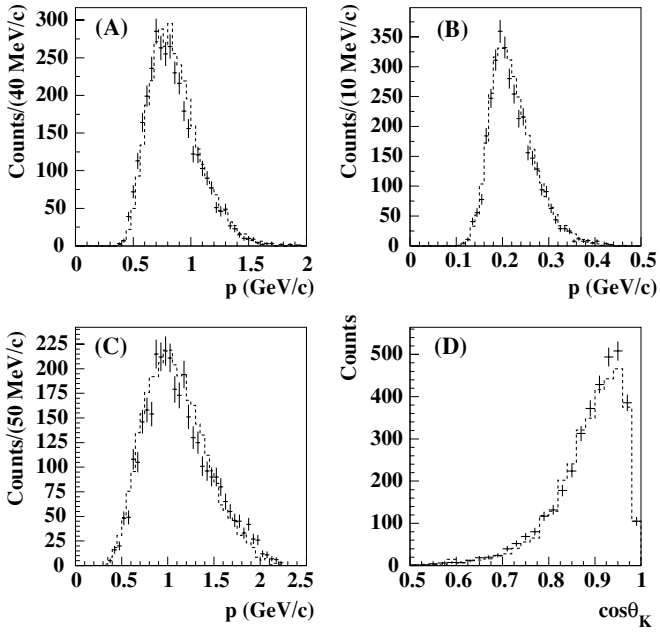

FIG. 15. Momentum and angular distributions for MC (dashed histograms) and data (points with error bars) for the 1.34–1.43-GeV hyperon mass region.

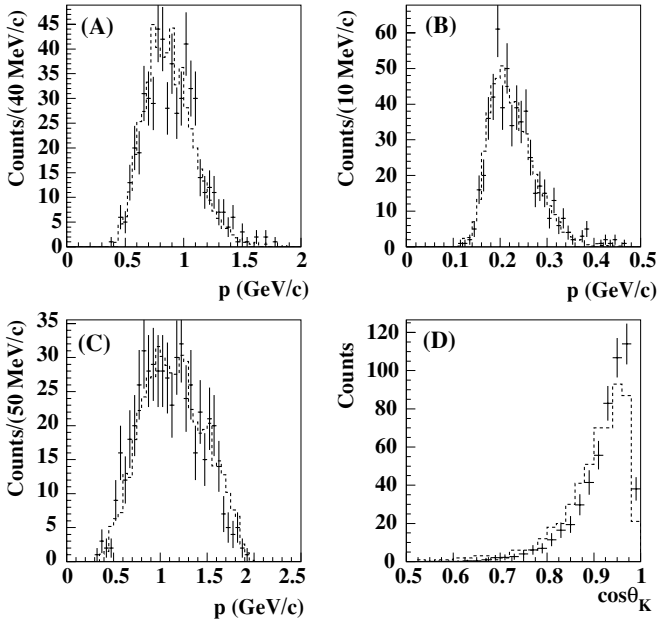

FIG. 16. Momentum and angular distributions for MC (dashed histograms) and data (points with error bars) for the 1.49–1.55 GeV hyperon mass region.

on the π^0 peak found in Fig. 14(A) to isolate the $\Sigma(1385) \to \Lambda\pi^0$ channel. We plotted the ratio of the data/MC versus photon energy $E_{\rm beam}$. The resultant curve was fitted with a function of the form $A/E_{\rm beam} + B/E_{\rm beam}^2$. We used this to modify the photon energy dependence of the $\Sigma(1385)$ production cross section in the MC. The above procedure was then iterated. The exponential slope parameter was varied until the MC and data t distributions matched reasonably well. The exponential slope for the modified t dependence was 1.0 GeV^{-2}. To check the quality of the simulation, we compared the momentum distributions for the MC and the data for the kaon, proton, and pion tracks. The simulated events were analyzed with the same cuts described above. The results for the second iteration for the MC simulation are shown in Fig. 15. The agreement between the MC and the data for the pion, proton, and kaon momenta and the kaon lab angle is good.

Figure 16 compares the data for the 1.49–1.55 GeV mass range and the missing mass squared in the range 0.018–0.075 GeV^2 to the $\Lambda(1520) \to \Sigma^0\pi^0$ MC results. The MC results have been scaled by 0.185. The agreement between the MC and the measured momenta distributions is very good, and the kaon angular distributions agree reasonably well.

To check that the $p_\perp^2$ cut did not introduce a bias of the MC results with respect to the data, we studied the yield of $\Sigma(1385) \to \Lambda\pi^0$ events in the data and the corresponding MC. For the data we used the standard χ^2 cuts and performed the same kind of fit to the hyperon mass distributions as described earlier. The hyperon mass range was 1.34–1.43 GeV. The results are tabulated in Table III. The data and the MC yields agree as a function of the $p_\perp^2$ cut.

Table II lists the acceptances for the case in which $\chi^2_{\rm HIGH} = \chi^2_{\rm LOW} = 3.841$. In the table A_π and A_γ refer to the fraction of surviving events relative to the number of thrown events that satisfy the $\Lambda\pi^0$ and $\Lambda\gamma$ hypotheses, respectively, and $A_{\gamma\pi}$ refers to those events that do not satisfy either hypothesis.

IV. $\Sigma^0(1385)$ ANALYSIS

To obtain the yields we fitted the hyperon mass distributions between 1.25 and 1.75 GeV. The yield of $\Lambda\pi^0$ events is extracted by fitting the data in Fig. 14(A) with a polynomial background and a relativistic Breit-Wigner of the form [28]

$$f(M) \propto \frac{2MM_0\Gamma(q)}{\left(M^2 - M_0^2\right)^2 + M_0^2\Gamma^2(q)}, \tag{10}$$

$$\Gamma(q) = \Gamma_0 \left(\frac{q}{q_0}\right)^{2l+1} \frac{M_0}{M} \left(\frac{X_0^2 + q_0^2}{X_0^2 + q^2}\right)^l, \tag{11}$$

$$q = \frac{\sqrt{\left(M^2 - M_\Lambda^2 - M_\pi^2\right)^2 - 4M_\Lambda^2 M_\pi^2}}{2M}, \tag{12}$$

$$q_0 = \frac{\sqrt{\left(M_0^2 - M_\Lambda^2 - M_\pi^2\right)^2 - 4M_\Lambda^2 M_\pi^2}}{2M_0}, \tag{13}$$

TABLE III. Comparison of yields between the $\Sigma(1385) \to \Lambda\pi^0$ simulation and the data as a function of the $p_\perp^2$ cut. The errors are statistical only.

$p_\perp^2$ cut (GeV^2)	N(data)	N(MC)	N(data)/N(MC)
0.005	4021	11037	0.364 ± 0.007
0.010	3500	9860	0.355 ± 0.007
0.015	2878	8148	0.353 ± 0.008
0.020	2191	6191	0.354 ± 0.009

where M_0 is the peak position of the resonance, $X_0 = 0.35$ GeV, and Γ_0 is the width. For the $\Sigma^* \to \Lambda\pi^0$ transition, $l = 1$. We tried both first-order and second-order polynomial background parametrizations. The systematic uncertainty in the yield extraction that was due to the choice of background function was about $\pm 1\%$. The mass and width of the $\Sigma(1385)$ were found to be 1.3860 and 0.03988 GeV, respectively. For the $\Lambda\gamma$ channel [Fig. 14(B)], we used two relativistic Breit-Wigners [one for the $\Sigma(1385)$ and one for the $\Lambda(1520)$] plus a polynomial background. The masses and widths were fixed to be those found from the fits to Figs. 14(A) and 14(D).

From Fig. 5(A) it is clear that we were not able to resolve the $\Lambda(1405)$ and the $\Sigma^0(1385)$; therefore, to find the number of $\Lambda(1405)$'s (n_Λ), we look at the events for which neither the γ nor the π^0 hypothesis is satisfied [Fig. 12(D)]. This isolated predominantly $\Lambda(1405) \to \Sigma^0\pi^0$ events, as the $\Sigma(1385) \to \Sigma^0\pi^0$ decay is forbidden by isospin. We parametrized the $\Lambda(1405)$ line shape by using the M-matrix formalism for S-wave $\Sigma^0\pi^0$ scattering below the $\overline{K}N$ threshold. The M matrix is related to the S-wave transition matrix T according to

$$T = Q^{\frac{1}{2}}(M - iQ)^{-1}Q^{\frac{1}{2}}, \tag{14}$$

where Q is a diagonal matrix containing the relative $\Sigma^0\pi^0$ momentum q and $\overline{K}N$ momentum k [29]. Note that, below the $\overline{K}N$ threshold, the latter is purely imaginary. The matrix M is expanded relative to the $\overline{K}N$ threshold $E_t = M_{\overline{K}} + M_N$ according to

$$M(E) = M(E_t) + \frac{1}{2}R[Q^2(E) - Q^2(E_t)]$$

$$= \begin{bmatrix} M_{11} & M_{12} \\ M_{12} & M_{22} \end{bmatrix}, \tag{15}$$

$$Q = \begin{bmatrix} k & 0 \\ 0 & q \end{bmatrix}, \tag{16}$$

$$R = \begin{bmatrix} R_{\overline{K}N} & 0 \\ 0 & R_{\Sigma\pi} \end{bmatrix}. \tag{17}$$

The amplitude for elastic scattering in the $\Sigma^0\pi^0$ channel is given by

$$T_{22} = \frac{q(M_{11} + |k|)}{(M_{11} + |k|)(M_{22} - iq) - M_{12}^2}. \tag{18}$$

Below E_t, the $\Sigma\pi$ mass spectrum is proportional to $|T_{22}|^2/q$. Figure 14(D) shows the M-matrix parametrization fit to the hyperon mass spectrum. A relativistic Breit-Wigner form is included to account for the leakage of the $\Sigma(1385) \to \Lambda\pi^0$ channel into the high missing mass squared region. A second relativistic Breit-Wigner is used for the $\Lambda(1520)$ contribution. The mass and width of the $\Lambda(1520)$ were found to be 1.520 and 0.022 GeV, respectively. We used a second-order polynomial for the remaining background beneath the peaks. The matrix elements at threshold and the effective ranges were determined from the fit to be $M_{11}(E_t) = 1.314$, $M_{12}(E_t) = -1.063$, $M_{22}(E_t) = 0.686$, $R_{\overline{K}N} = 9.543$, and $R_{\Sigma\pi} = -28.89$. We find 328 ± 36 $\Lambda(1405)$ counts and 245 ± 37 $\Sigma(1385)$ counts in the hyperon mass region 1.34–1.43 GeV. The reduced χ^2 for the fit was 0.866.

Although the π^0 leakage into the γ channel is the dominant correction to the branching ratio, the final result still needs corrections for $\Sigma^+\pi^-$ contamination and the contribution to the numerator from the reaction $\Lambda(1405) \to \Lambda\gamma$. From the measured 27 ± 8-keV radiative width [19], we assume that the leakage of the $\Sigma\gamma$ channel into the γ region is small relative to the $\Lambda\gamma$ signal and that the leakage into the π^0 region is small compared with the $\Lambda\pi^0$ signal. The formula for the acceptance corrected branching ratio is

$$R = \frac{1}{\Delta n_\pi A_\gamma^\Sigma(\Lambda\gamma) - \Delta n_\gamma A_\pi^\Sigma(\Lambda\gamma)} \times \left\{ \Delta n_\gamma \left[A_\pi^\Sigma(\Lambda\pi) + \frac{R_{\Lambda\pi}^{\Sigma\pi}}{2} A_\pi^\Sigma(\Sigma\pi) \right] - \Delta n_\pi \left[A_\gamma^\Sigma(\Lambda\pi) + \frac{R_{\Lambda\pi}^{\Sigma\pi}}{2} A_\gamma^\Sigma(\Sigma\pi) \right] \right\}, \tag{19}$$

$$\Delta n_\pi = n_\pi - N_\pi(\Lambda^* \to \Sigma^+\pi^-) - N_\pi(\Lambda^* \to \Sigma^0\pi^0) - N_\pi(\Lambda^* \to \Sigma^0\gamma) - N_\pi(\Lambda^* \to \Lambda\gamma), \tag{20}$$

$$\Delta n_\gamma = n_\gamma - N_\gamma(\Lambda^* \to \Sigma^+\pi^-) - N_\gamma(\Lambda^* \to \Sigma^0\pi^0) - N_\gamma(\Lambda^* \to \Sigma^0\gamma) - N_\gamma(\Lambda^* \to \Lambda\gamma), \tag{21}$$

where n_γ (n_π) is the measured number of photon (pion) candidates and the remaining $N_{\gamma,\pi}$ terms are corrections that are due to leakage from the $\Lambda(1405)$. The acceptance for the individual pion (photon) channels are denoted as $A_\pi^\Sigma(\Sigma^+\pi^-)$, $[A_\gamma^\Sigma(\Sigma^+\pi^-)]$ and so on. For example, $A_\gamma^\Sigma(\Lambda\pi)$ denotes the relative leakage of the $\Lambda\pi$ channel into the $\Lambda\gamma$ channel. Table II lists the values of these "acceptances."

The corrections depend on an estimate of the number n_Λ of $\Lambda(1405)$'s in the data set. They are

$$N_\gamma(\Lambda^* \to \Lambda\gamma) = \frac{A_\gamma^\Lambda(\Lambda\gamma)R(\Lambda^* \to \Lambda\gamma)n_\Lambda}{A_{\gamma\pi}^\Lambda(\Sigma^0\pi^0) + A_{\gamma\pi}^\Lambda(\Sigma^+\pi^-)}, \tag{22}$$

$$N_\gamma(\Lambda^* \to \Sigma^0\gamma) = \frac{A_\gamma^\Lambda(\Sigma^0\gamma)R(\Lambda^* \to \Sigma^0\gamma)n_\Lambda}{A_{\gamma\pi}^\Lambda(\Sigma^0\pi^0) + A_{\gamma\pi}^\Lambda(\Sigma^+\pi^-)}, \tag{23}$$

$$N_\gamma(\Lambda^* \to \Sigma^0\pi^0) = \frac{A_\gamma^\Lambda(\Sigma^0\pi^0)n_\Lambda}{A_{\gamma\pi}^\Lambda(\Sigma^0\pi^0) + A_{\gamma\pi}^\Lambda(\Sigma^+\pi^-)}, \tag{24}$$

$$N_\gamma(\Lambda^* \to \Sigma^+\pi^-) = \frac{A_\gamma^\Lambda(\Sigma^+\pi^-)n_\Lambda}{A_{\gamma\pi}^\Lambda(\Sigma^0\pi^0) + A_{\gamma\pi}^\Lambda(\Sigma^+\pi^-)}, \tag{25}$$

and similarly for the pion channel. Here isospin symmetry is assumed such that $R(\Sigma^0\pi^0) = R(\Sigma^+\pi^-) = R(\Sigma^-\pi^+) \approx 1/3$ for the $\Lambda(1405)$ decay channels. The subscript "$\gamma\pi$" refers to those events for which both a pion and a photon are missing or those events leaking into the "$\gamma\pi$" region because of the tail of the π^0 peak (this is why the $\Sigma^+\pi^-$ contamination must be included in the denominator, although

TABLE IV. Breakdown of statistics for the $\Lambda\gamma$ and $\Lambda\pi^0$ channels. The errors are statistical only.

Reaction	Yield
Estimated $\Sigma^0\pi^0$ counts	373.8 ± 34.0
Raw π^0 counts	2878.3 ± 77.4
$\Lambda(1405) \to \Sigma^0\gamma$	0.45 ± 0.17
$\Lambda(1405) \to \Sigma\pi$	95.7 ± 9.5
$\Sigma(1385) \to \Sigma\pi$	10.4 ± 1.0
$\Sigma(1385) \to \Lambda\gamma$	0.87 ± 0.21
Corrected π^0 counts	2770.9 ± 78.0
Raw γ counts	100.2 ± 15.4
$\Sigma(1385) \to \Lambda\pi^0$	35.0 ± 1.0
$\Sigma(1385) \to \Sigma^+\pi^-$	0.38 ± 0.3
$\Lambda(1405) \to \Lambda^0\gamma$	0.85 ± 0.27
$\Lambda(1405) \to \Sigma^0\gamma$	0.29 ± 0.11
$\Lambda(1405) \to \Sigma\pi$	2.47 ± 0.25
Corrected γ counts	61.2 ± 15.4

the leakage for this channel is small). Table IV lists the yields for the various channels of the $\Sigma(1385)$ decays. The hyperon mass range was 1.34–1.43 GeV. The reaction $\gamma p \to \Lambda K^{*+}$ causes a smooth background underneath the $\Sigma(1385)$ peak in Figs. 14(A) and 14(B) that is well parametrized by the second-order polynomial fit. Hence it has not been explicitly included in Table IV. The largest background in the γ channel is due to leakage of the π^0 tail into the γ missing mass squared region.

After subtracting the background contributions enumerated in Table IV there were 61.2 ± 15.4 counts consistent with $\Sigma^0(1385) \to \Lambda\gamma$ and 2770.9 ± 78.0 counts consistent with $\Sigma^0(1385) \to \Lambda\pi^0$. After correcting for the relative acceptance of the two channels, we obtained a branching ratio, $R^{\Lambda\gamma}_{\Lambda\pi}$, of

$$\frac{\Gamma[\Sigma^0(1385) \to \Lambda\gamma]}{\Gamma[\Sigma^0(1385) \to \Lambda\pi^0]} = 1.53 \pm 0.39(\text{stat})\%. \qquad (26)$$

The branching ratio result for the $\Sigma(1385)$ depends on how well we understand the tail of the π^0 peak near the γ peak. Figures 17(C) and 17(D) show the comparison between the data and the MC for the reaction $Y^* \to \Lambda X$ for the 1.34–1.43-GeV hyperon mass region. The excess of counts above the π^0 peak correspond to $Y \to \Sigma^0\pi^0$, where $\Sigma^0 \to \Lambda\gamma$. Although the $Y \to \Lambda\gamma$ decay is not completely separated, a clear enhancement near zero missing mass squared can be seen above the π^0 tail, clearly indicating the presence of radiative events. The MC predicts that the leakage accounts for about 30% of the raw photon yield in the $|M_X^2| < 0.01$ GeV^2 region. To assess the quality of the MC in the tail, we looked at $\Lambda(1405) \to \Sigma^+\pi^-$ events for which the Σ^+ subsequently decayed to $p\pi^0$. We chose this channel because there are no channels that can distort the spectrum above the π^0 peak, the Σ^+ radiative channel is rare ($BR = 1.25 \times 10^{-3}$), and it has similar kinematics to those of the $\Lambda\pi^0$ decay. We required the $p\pi^-$ invariant mass to be greater than 1.13 GeV [to eliminate the $\Lambda(1116)$ from the sample]. To identify the

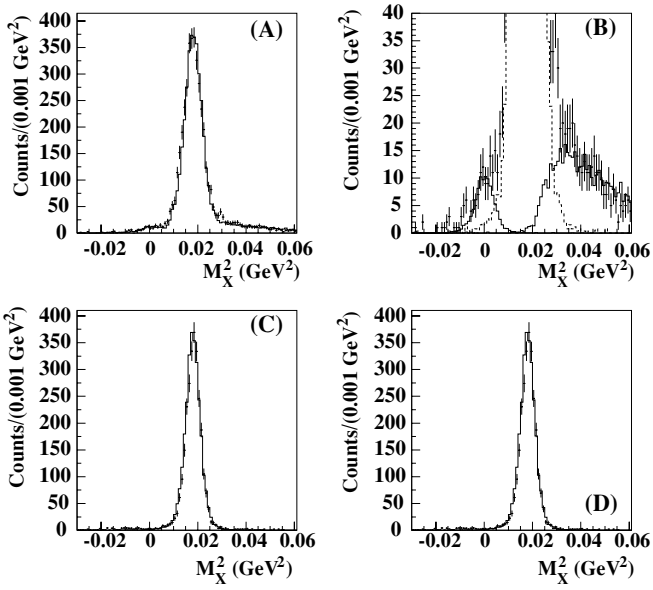

FIG. 17. Comparison between data and MC results for the reactions and $Y^* \to \Lambda X$ (top histograms) and $Y^* \to \Sigma^+\pi^-$ (bottom histograms) after kinematic fitting has been performed. The points with error bars are the data, and the curves are the MC results. Histograms (B) and (D) have the vertical scales expanded by a factor of 10. In (B) the solid curve on the left is the $\Sigma^* \to \Lambda\gamma$ simulation, the central dashed curve is the $\Sigma^* \to \Lambda\pi^0$ simulation, the solid curve on the right is the $\Lambda(1405) \to \Sigma^0\pi^0$ simulation. In (A) the curve is the sum of the three. In (C) and (D) the $\Sigma^+\pi^-$ data and the $\Sigma(1385) \to \Lambda\pi^0$ MC distribution have been scaled to agree with the peak height of the π^0 in the $Y^* \to \Lambda X$ distribution from the data set.

$\Sigma^+(1189)$ we required the pX invariant mass (or, equivalently, the missing mass recoiling off the $K^+\pi^-$ system) to be in the range 1.17–1.206 GeV. We performed kinematic fits on these events with vertex and four-momentum conservation constraints. Explicitly, the constraint equations are

$$\vec{f} = \begin{bmatrix} E_{\text{beam}} + m_p - E_K - E_\pi - E_{\Sigma^+} \\ \vec{p}_{\text{beam}} - \vec{p}_\pi - \vec{p}_p - \vec{p}_{\Sigma^+} \\ (y - y_\pi)p_\pi^z - (z - z_\pi)p_\pi^y \\ (x - x_\pi)p_\pi^z - (z - z_\pi)p_\pi^x \\ (y - y_p)p_K^z - (z - z_p)p_K^y \\ (x - x_p)p_K^z - (z - z_p)p_K^x \end{bmatrix} = \vec{0}. \qquad (27)$$

The missing mass squared distribution for the reaction chain $Y^* \to \Sigma^+\pi^-$, $\Sigma^+ \to p(X)$ is shown in Figs. 17(C) and 17(D) for hyperon masses in the 1.38–1.45-GeV mass region. We used the four-vector for the Σ^+ obtained from the fit, with less than 0.5% probability of exceeding χ^2. The MC result (dashed histograms) for the $\Lambda(1405) \to \Sigma^+\pi^-$ reaction agrees very well with the data down to about zero missing mass squared. The discrepancy between the MC and the data in the -0.01 to $+0.01$ GeV^2 region is $\sim$19%. Scaling the leakage of the $\Lambda\pi^0$ channel into the γ region by a factor of 1.19 reduces the branching ratio from 1.53% to 1.36% for a relative change of about -11%. More importantly, a comparison of Fig. 17(B) with Fig. 17(D) shows a clear enhancement at zero missing mass present for the latter case not in evidence for the former

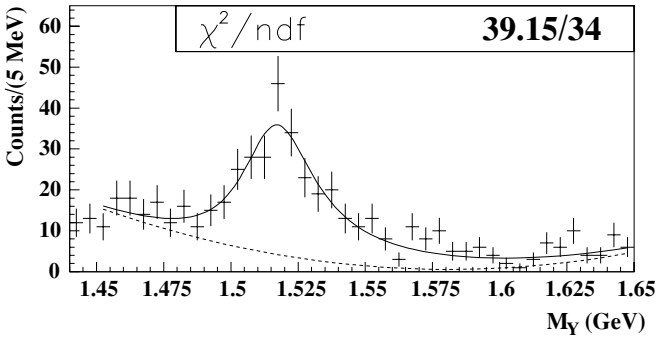

FIG. 18. Sample fit of the ΛX mass distribution for missing mass squared in the 0.018–0.075-GeV^2 range.

case. The negative systematic error will be increased by 11% in quadrature.

V. $\Sigma^0(1520)$ ANALYSIS

For the $\Lambda(1520)$ analysis we calculated the radiative branching ratio relative to the $\Sigma^0\pi^0$ and the $\Sigma^+\pi^-$ channels. The hyperon mass cut used to identify the $\Lambda(1520)$ was 1.49–1.55 GeV. From the fit to the histogram shown in Fig. 14, we obtained $n_\gamma = 32.5 \pm 8.2$. To identify the $\Sigma^0\pi^0$ channel we used events for which neither the γ nor the π^0 hypothesis is satisfied. The ground state Λ is a decay product in the $\Sigma^0\pi^0$ (14%) and $\Lambda\pi\pi$ (10%) channels. To simplify the calculation for the branching ratio we require the missing mass squared to be in the range between $m^2_{\pi^0}$ and 0.075 GeV^2 ($\approx 4m^2_{\pi^0}$, the two-pion threshold). This isolates the $\Sigma^0\pi^0$ channel. The hyperon mass distribution in the $\Lambda(1520)$ region with this additional cut applied is shown in Fig. 18. The fit is a D wave ($l = 2$) relativistic Breit-Wigner plus a polynomial background. We tried both first-order and second-order polynomials; the results for the yield differed by $\pm 1.6\%$. The leakage of one channel into the other is neglible and applying the correction does not change the result. Because of the low acceptance for events containing Λ's, the raw number of $\Sigma^0\pi^0$ counts is only a factor of 6 larger than the radiative signal and the technique relies on isolating a channel for which two particles (γ and π^0) are not detected. We also looked at $\Lambda(1520) \to \Sigma^+\pi^-$ events for which the acceptance is higher. The same particle identification and vertex cuts used for the previous analysis were applied with some modifications. We required that the $p\pi^-$ invariant mass be greater than 1.13 GeV to cut $\Lambda(1116)$ contamination. The primary vertex was determined with the K^+ and π^- tracks. The z position and x and y positions for these vertexes are shown in Figs. 19(A) and 19(B), respectively. A prominent $\Sigma^+(1189)$ peak shows up in the missing mass, recoiling against the K^+ and the π^- [Fig. 19(C)]. The hyperon mass spectrum for those events in the range 1.165–1.215 GeV about the Σ^+ peak is shown in Fig. 19(D). The curve is a fit to the $\Lambda(1520)$ region by use of a D-wave relativistic Breit-Wigner with a second-order polynomial background. In the region between 1.49 and 1.55 GeV we obtain $n_{\Lambda^*} = 5290 \pm 124$ (the acceptance of CLAS is much larger for this channel than the others because of the larger π^- momentum). The yields for these two reactions

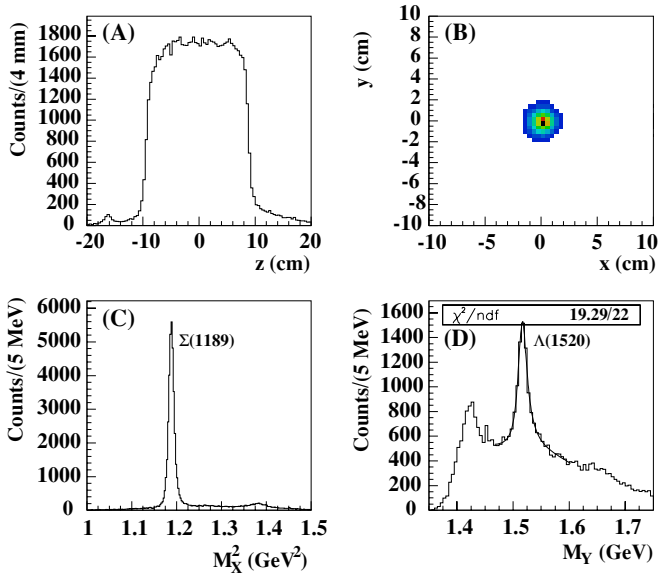

FIG. 19. (Color online) Isolation of $Y^* \to \Sigma^+\pi^-$ events. (A) and (B) show the $K^+\pi^-$ vertex distributions. (C) is the missing mass for the reaction $\gamma p \to K^+\pi^- X$. (D) is the hyperon mass distribution for events satisfying the Σ^+ identification cut (see text).

are listed in Table V. As can be seen from the numbers in the table the leakage of each channel into the other is negligible. None of the generated $\Lambda(1520) \to \Sigma^+\pi^-$ events satisfied the selection criteria. There is no $\Lambda\pi^0$ leakage because this channel is forbidden by isospin.

We obtained a raw branching ratio of $n_\gamma/n_{\gamma\pi} = 16.0 \pm 4.3\%$. Correcting for acceptance, we found that the branching ratio is

$$\frac{\Gamma(\Lambda\gamma)}{\Gamma(\Sigma^0\pi^0)} = \frac{A_{\gamma\pi}(\Sigma^0\pi^0)}{A_\gamma(\Lambda\gamma)} \frac{n_\gamma}{n_{\gamma\pi}} = 7.9 \pm 2.1\%. \qquad (28)$$

The acceptances used in this calculation are listed in Table II. To obtain the branching ratio $\Gamma(\Lambda\gamma)/\Gamma_{\rm TOT}$ we scale this result by the branching fraction of 14% for the $\Sigma^0\pi^0$ channel (assuming isospin symmetry) to obtain $1.10 \pm 0.29\%$. The acceptance for the $\Lambda(1520) \to \Sigma^+\pi^-$ channel was $1.66 \pm 0.06\%$. We obtain $1.01 \pm 0.26\%$ for the radiative

TABLE V. Breakdown of statistics for the $\Lambda(1520)$ analysis. The errors are statistical only.

Reaction	Yield
$\Lambda(1520) \to \Sigma^+\pi^-$	5290 ± 124
$\Lambda(1520) \to \Sigma^0\pi^0$	202.8 ± 16.7
$\Lambda(1520) \to \Lambda\gamma$	0.05 ± 0.01
Corrected π^0 counts	202.8 ± 16.7
Raw γ counts	32.5 ± 8.2
$\Lambda(1520) \to \Sigma^0\pi^0$	0.09 ± 0.01
Corrected γ counts	32.4 ± 8.2

TABLE VI. Dependence of the $\Sigma(1385) \to \Lambda\gamma$ and $\Lambda(1520) \to \Lambda\gamma$ branching ratios on the choice of $\chi^2_{\mathrm{HIGH,\,LOW}}$ cuts.

χ^2_{LOW}	χ^2_{HIGH}	R(%) $\Sigma(1385)$	R(%) $\Lambda(1520)$
2.706	2.706	1.68 ± 0.41	1.20 ± 0.29
3.841	3.841	1.53 ± 0.39	1.10 ± 0.29
6.635	6.635	1.58 ± 0.40	1.13 ± 0.33
2.706	6.635	1.38 ± 0.38	1.25 ± 0.33
3.841	6.635	1.36 ± 0.30	1.06 ± 0.34

branching ratio. The results for the two channels agree after acceptance corrections.

If contamination that is due to the $\Lambda(1520) \to \Sigma^0\gamma$ channel is present, the branching ratio for the $\Lambda\gamma$ channel acquires a small correction term:

$$R(\Lambda\gamma) = \frac{A_{\gamma\pi}(\Sigma^0\pi^0)}{A_\gamma(\Lambda\gamma)}\frac{n_\gamma}{n_{\gamma\pi}}R(\Sigma^0\pi^0) + R(\Sigma^0\gamma)\left(\frac{A_{\gamma\pi}(\Sigma^0\gamma)n_\gamma - A_\gamma(\Sigma^0\gamma)n_{\gamma\pi}}{A_\gamma(\Lambda\gamma)n_{\gamma\pi}}\right), \tag{29}$$

where $R(\Sigma^0\gamma)$ is the branching ratio to the $\Sigma^0\gamma$ channel and $R(\Sigma^0\pi^0)$ is the branching ratio to the $\Sigma^0\pi^0$ channel. Using the largest theoretical estimate for the $\Sigma^0\gamma$ radiative width of 293 keV from Warns, Pfeil, and Rollnik, [5], we obtain a correction of $+0.01\%$. Therefore this contamination can be neglected.

VI. RESULTS

To check the sensitivity to the confidence limits used, $R^{\Lambda\gamma}_{\Lambda\pi^0}$ was calculated with 1%, 5%, and 10% probability for accepting a channel and 99%, 95%, and 90% probability for rejecting a channel. Table VI lists the corrected branching ratios as a function of the $\chi^2_{\mathrm{HIGH,LOW}}$ cuts. The third column in Table VI gives the $\Sigma(1385)$ results. The results were very stable, varing from $+0.15$ (10%, 90%) to -0.17 (5%, 99%). These values were used as estimates of the systematic errors. The value for the branching ratio is $1.53 \pm 0.39(\mathrm{stat})^{+0.15}_{-0.17}(\mathrm{sys})\%$, where the second uncertainty reflects the variation in the branching ratio as a function of the choice of χ^2 cuts.

We add the 11% relative error (i.e., -0.17% absolute) that could result from underestimating the tail of the π^0 response to the negative systematic error and quote a branching ratio of $1.53 \pm 0.39(\mathrm{stat})^{+0.15}_{-0.24}(\mathrm{sys})\%$. The positive systematic error reflects the range of values we obtained for the various estimates for the branching ratio. If we neglect the small (unmeasured) contribution that is due to the $\Sigma^0\gamma$ channel, the $\Sigma^0(1385) \to \Lambda\gamma$ partial width is given by

$$\Gamma(\Lambda\gamma) = \frac{R^{\Lambda\gamma}_{\Lambda\pi}\Gamma_{\mathrm{TOT}}}{1 + R^{\Lambda\gamma}_{\Lambda\pi} + R^{\Sigma\pi}_{\Lambda\pi}} = 479 \pm 120(\mathrm{stat})^{+81}_{-100}(\mathrm{sys})\,\mathrm{keV}, \tag{30}$$

using $\Gamma_{\mathrm{TOT}} = 36 \pm 5$ MeV and $R^{\Sigma\pi}_{\Lambda\pi} = 0.135 \pm 0.011$, the branching ratio of the $\Sigma\pi$ channels relative to the $\Lambda\pi^0$ channel [30]. The errors on Γ_{TOT} and $R^{\Sigma\pi}_{\Lambda\pi}$ are included in the systematic error for $\Gamma(\Lambda\gamma)$. If we use the largest theoretical estimate for the $\Sigma^0\gamma$ channel relative to the $\Lambda\gamma$ channel of 0.153 from R. Bijker, F. Iachello, and A. Leviatan [11], the partial width is reduced to 478 keV, which is an insignificant change.

For the $\Lambda(1520)$ decay, we obtained a branching ratio of $1.10 \pm 0.29(\mathrm{stat})^{+0.15}_{-0.04}(\mathrm{sys})\%$ by using the $\Sigma^0\pi^0$ channel and $1.01 \pm 0.27\%$ by using the $\Sigma^+\pi^-$ channel. The weighted average gives a branching ratio of

$$\frac{\Gamma[\Lambda(1520) \to \Lambda\gamma]}{\Gamma_{\mathrm{TOT}}} = 1.07 \pm 0.29(\mathrm{stat})^{+0.15}_{-0.04}(\mathrm{sys})\%. \tag{31}$$

Table VI lists the branching ratios for various combinations of kinematic fitting χ^2 cuts. There is no obvious dependence on the choice of cuts. To determine the systematic error in the measurement by using the $\Sigma^0\pi^0$ channel to normalize, we used the range of branching ratio values obtained for different choices of χ^2 cuts. Using a full width of 15.6 ± 1 MeV [30], we obtained a partial width of $167 \pm 43(\mathrm{stat})^{+26}_{-12}(\mathrm{sys})$ keV. The error on the full width is included in the systematic error for $\Gamma(\Lambda\gamma)$. The $\Lambda(1520)$ result is compatible with the result of Mast *et al.* [16] and the result of Antipov *et al.* [18] but disagrees with the result of Bertini *et al.* [17]. Together, our result and those of Mast *et al.* and Antipov *et al.* exclude the bag models listed in Table I.

The $\Sigma^0(1385) \to \Lambda\gamma$ channel has never been measured before. The result is roughly 2–3 times larger than all of the existing model predictions except for HBχPT [12]. Table I reveals that the model predictions for the $\Delta \to p\gamma$ transition are also about 50% low. Sato and Lee [31] showed that much of that discrepancy could be accounted for by the inclusion of non-resonant meson exchange effects. They found a width of 530 ± 45 keV, about 80% of the experimental value. Lu, Thomas, and Williams [32] reproduced the $\Delta \to p\gamma$ data by using a chiral bag model calculation with a relatively small bag radius of 0.7 fm. About 40% of the transition was due to the pion cloud. These calculations suggest that mesonic effects could account for the discrepancy between the model predictions and our result for the $\Sigma^0(1385)$ radiative transition.

ACKNOWLEDGMENTS

We would like to acknowledge the outstanding efforts of the staff of the Accelerator and the Physics Divisions at the Thomas Jefferson National Accelerator Facility who made this experiment possible. This work was supported in part by the Istituto Nazionale di Fisica Nucleare, the French Centre National de la Recherche Scientifique, the French Commissariat à l'Energie Atomique, the U.S. Department of Energy, the National Science Foundation, Emmy Noether grant from the Deutsche Forschungs Gemeinschaft, and the Korean Science and Engineering Foundation. The Southeastern Universities Research Association operates the Thomas Jefferson National Accelerator Facility for the United States Department of Energy under contract DE-AC05-84ER40150.

[1] S. P. Barrow *et al*., Phys. Rev. C **64**, 044601 (2001).
[2] N. Isgur and G. Karl, Phys. Rev. D **18**, 4187 (1978); **20**, 1191 (1979).
[3] E. Kaxiras, E. J. Moniz, and M. Soyeur, Phys. Rev. D **32**, 695 (1985).
[4] J. W. Darewych, M. Horbatsch, and R. Koniuk, Phys. Rev. D **28**, 1125 (1983).
[5] M. Warns, W. Pfeil, and H. Rollnik, Phys. Lett. **B258**, 431 (1991).
[6] G. Wagner, A. J. Buchmann, and A. Faessler, Phys. Rev. C **58**, 1745 (1998).
[7] Y. Umino and F. Myhrer, Nucl. Phys. **A529**, 713 (1993); **A554**, 593 (1993).
[8] C. L. Schat, C. Gobbi, and N. B. Scoccola, Phys. Lett. **B356**, 1 (1995).
[9] A. Abada, H. Weigel, and H. Reinhardt, Phys. Lett. **B366**, 26 (1996).
[10] T. Haberichter, H. Reinhardt, N. N. Scocoola, and H. Weigel, Nucl. Phys. **A615**, 291 (1997).
[11] R. Bijker, F. Iachello, and A. Leviatan, Ann. Phys. (NY) **284**, 89 (2000).
[12] M. N. Butler, M. J. Savage, and R. P. Springer, Nucl. Phys. **B399**, 69 (1993).
[13] R. F. Lebed and D. R. Martin, Phys. Rev. D **70**, 057901 (2004).
[14] R. Koniuk and N. Isgur, Phys. Rev. D **21**, 1868 (1980); **23**, 818(E) (1981).
[15] L. G. Landsberg, Phys. At. Nucl. **59**, 2080 (1996).
[16] T. S. Mast, M. Alston-Garnjost, R. O. Bangerter, A. Barbaro-Galtieri, L. K. Gerswhwin, F. T. Solmitz, and R. D Tripp, Phys. Rev. Lett. **21**, 1715 (1968).
[17] R. Bertini, Nucl. Phys. **B279**, 49 (1987); R. Bertini *et al*., SACLAY-DPh-N-2372 (unpublished).
[18] Y. M. Antipov *et al*. (SPHINX Collaboration), Phys. Lett. **B604**, 22 (2004).
[19] H. Burkhardt and J. Lowe, Phys. Rev. C **44**, 607 (1991).
[20] D. A. Whitehouse *et al*., Phys. Rev. Lett. **63**, 1352 (1989).
[21] G. W. Meisner, Nuovo Cimento A **12**, 62 (1972).
[22] J. Colas, C. Farwell, A. Ferrer, and J. Six, Nucl. Phys. **B91**, 253 (1975).
[23] D. I. Sober *et al*., Nucl. Instrum. Methods A **440**, 263 (2000).
[24] B. A. Mecking *et al*., Nucl. Instrum. Methods A **503**, 513 (2003).
[25] S. Taylor, S. Ahmed, J. Distelbrink, G. S. Mutchler, E. Smith, and T. Smith, Nucl. Instrum. Methods A **462**, 484 (2001).
[26] A. G. Frodesen, O. Skjeggestad, and H. Tøfte, *Probability and Statistics in Particle Physics* (Universitetsforlaget, Bergen, Norway, 1979).
[27] J. C. Nacher, E. Oset, H. Toki, and A. Ramos, Phys. Lett. **B455**, 55 (1999).
[28] J. D. Jackson, Nuovo Cimento **34**, 1644 (1964).
[29] D. W. Thomas, A. Engler, H. E. Fisk, and R. W. Kraemer, Nucl. Phys. **B56**, 15 (1973).
[30] K. Hagiwara *et al*., Particle Data Group, Phys. Rev. D **66**, 010001 (2002).
[31] T. Sato and T. S.-H. Lee, Phys. Rev. C **54**, 2660 (1996).
[32] D. H. Lu, A. W. Thomas, and A. G. Williams, Phys. Rev. C **55**, 3108 (1992).